Fabry-Perot Resonances in Bilayer Metasurfaces

G. Alagappan,[1,*] F. J. García-Vidal,[1,2] and C. E. Png[1]
[1]Institute of High-Performance Computing, Agency for Science, Technology, and Research (A-STAR), Fusionopolis, 1 Fusionopolis Way, #16-16 Connexis, Singapore 138632, Singapore
[2]Departamento de Física Teórica de la Materia Condensada and Condensed Matter Physics Center (IFIMAC), Universidad Autónoma de Madrid, E-28049 Cantoblanco, Madrid, Spain

(Received 22 May 2024; accepted 8 October 2024; published 25 November 2024)

In this study, we construct Fabry-Perot cavities in which nanostructured, thin resonant metasurfaces act as mirrors. We develop a temporal coupled-mode theory and provide an accurate description of the resonances supported by these cavities, deriving analytically their transmission characteristics. The presence of metasurface mirrors introduces a substantial group delay, causing the field concentration to shift from the bulk of the cavity towards the regions close to the two metasurfaces. This shift is accompanied by a significant increase in the quality factor of the resonances that is associated with the emergence of singular points in frequency space. These singular points exist even when the cavity separations are smaller than the cavity length of the fundamental mode in standard cavities, enabling meta-mirror Fabry-Perot cavities to outperform traditional cavities by achieving much higher quality factors despite displaying shorter cavity lengths.

DOI: 10.1103/PhysRevLett.133.226901

Traditional Fabry-Perot (FP) cavities [1–7] consist of two parallel reflective surfaces, typically metallic or dielectric, which do not support resonances. When the distance between these mirrors matches the resonance condition, the reflected light beams interfere coherently, creating standing wave patterns within the cavity. On the other hand, metasurfaces—quasi-two-dimensional nanoscale metamaterials, have revolutionized flat-optics technology [8,9]. They have enabled the creation of ultrathin planar optical devices [10–14]. Dielectric metasurfaces, in particular, are attractive for semiconductor photonics as they eliminate intrinsic losses associated with plasmonic metasurfaces in the optical regime, thereby enhancing efficiency [15–17]. These metasurfaces can be fabricated using conventional photonic technologies and integrated into photonic circuits [18,19]. Embedding a thin metasurface in a standard FP cavity with metallic mirrors can reduce cavity thickness for color filtering [20]. Reflective metasurfaces have been also integrated with hollow core fibers to form FP cavities. In such systems, metasurfaces serve merely as mirrors of high reflectivity [21] and, consequently, the underlying physics follows that of traditional FP cavities.

In this Letter, we demonstrate that replacing traditional reflective mirrors in FP cavities with thin dielectric metasurfaces exhibiting dielectric resonances [22–24] introduces new functionalities. Unlike nonresonant mirrors, each metasurface in these meta-mirror FP cavities supports a resonance characterized by a finesse coefficient F and a quality factor Q_s. Using a temporal coupled-mode formalism, we analytically derive the transmission characteristics of the meta-mirror FP system, presenting a unified theory applicable to both resonating and nonresonating mirrors, as well as short and long cavities. In meta-mirror FP cavities, the electromagnetic field predominantly concentrates at the thin metasurface regions rather than the bulk of the cavity, relevant for practical applications. This shift in field distribution is accompanied by a significant increase in the quality factor of the resonances that is associated with the emergence of singular points in frequency space. We discover that resonant meta-mirrors provide an additional mechanism to the overall quality factor, scaling as $Q_s\sqrt{F}$, independent of the cavity length. We identify three cavity length regimes based on resonance nature and quality factor, marked by two fundamental characteristic lengths. The first regime exhibits Fano resonances, while the second and third show induced transparencies with Lorentzian lineshapes. In the second regime, peak sharpness is determined by the quality factor of a single metasurface. In the third regime, the quality factor varies linearly with cavity length, similar to traditional cavities.

Resonant dielectric metasurfaces are usually built up by a periodic array of dielectric scatterers with a period a. We start by examining a single layer of a resonant metasurface exhibiting a transmission dip at an angular frequency ω_s. As an example, we consider a silicon metasurface with $a = 1$ μm and a typical membrane thickness of $h = 0.22a$ embedded in silica, and whose unit cells are circular nanodisks of radii r. Isolated transmission dips can be

*Contact author: gandhi@ihpc.a-star.edu.sg

observed in the spectrum for r ranging from $0.15a$ to $0.2a$, which exhibit Lorentzian line shapes and are attributed to isolated dielectric resonances [24]. Similar to other resonant systems in photonics, this isolated resonance can be characterized using a temporal coupled mode formalism [25–29]. This formalism establishes relationships between the electric field amplitude within the metasurface A and the amplitudes of the electric fields associated with the incoming $[s_1, s_2]$ and outgoing $[q_1, q_2]$ waves [see Fig. 1(a)]. The rate of amplitude growth within the metasurface is described by the equation $(dA/dt) = (j\omega_s - \Gamma)A + c_s s_1 + c_s s_2$, where Γ represents the decay rate, and c_s is the coupling coefficient accounting for the coupling of incoming waves s_1 and s_2 from both sides of the metasurface. The outgoing amplitudes are given by $q_1 = e^{j\gamma} s_2 + c_a A$ and $q_2 = e^{j\gamma} s_1 + c_a A$, where γ is a phase factor. This phase factor accounts for the phase that an incoming wave would acquire when passing through the metasurface if the resonance would not be present as, in this case, the metasurface would display a unitary transmissivity, $|q_2|^2 = |s_1|^2$. As shown below, this phase factor is critical in determining the transmission characteristics of the bilayer system. Utilizing time reversal symmetry, and assuming no intrinsic losses, it can be demonstrated that $c_s c_a = -e^{j\gamma}\Gamma$ and $|c_a|^2 = \Gamma$ (see Supplemental Material [30] for details). The electric field transmission and reflection coefficients can be then derived by applying Fourier transforms to the aforementioned equations. For a single metasurface, these coefficients can be expressed as $t_s(\omega) = (q_2/s_1)|_{s_2=0} = [j\delta e^{j\gamma}/(j\delta + \Gamma)]$ and $r_s(\omega) = (q_1/s_1)|_{s_2=0} = -[\Gamma e^{j\gamma}/(j\delta + \Gamma)]$, respectively. Here, $\delta = \omega - \omega_s$, where $\omega = 2\pi c/\lambda$ is the angular frequency with c and λ being the speed of light and the freespace wavelength, respectively. The decay rate Γ (due to the coupling to the external radiation modes) can be accurately estimated from the numerically evaluated transmission spectrum of the metasurface and it is given by $\Gamma = (\omega_s/2Q_s)$. In Fig. 1(b), we plot the transmission spectrum of the silicon metasurface with $r = 0.15a$ as a function of normalized frequency, $\omega a/2\pi c = a/\lambda$. As we can see from this figure, there are two transmission dips at normalized frequencies 0.677 and 0.687. The theoretical fit for the first resonance is shown in dark yellow, whereas the fit for the second resonance is shown in the inset. This figure demonstrates the good agreement between the analytical expressions derived from the temporal coupled mode formalism and three-dimensional (3D) finite-difference time-domain (FDTD) calculations [31]. Notice that, as we are interested on the spectral region between normalized frequencies 0.665 and 0.685 (see below), from now on we will use the fitting parameters associated with the first resonance located at 0.677.

For a bilayer made of resonant metasurfaces separated by a distance L, we can develop temporal coupled mode equations by working with the electric field amplitudes in the two metasurfaces, A_1 and A_2. In isolation, these

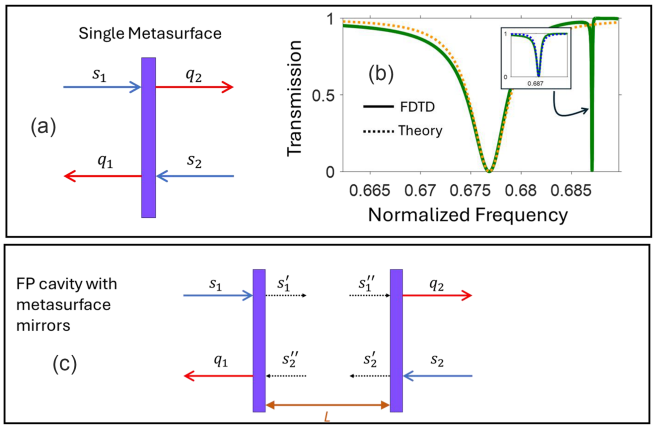

FIG. 1. (a) Schematics of a metasurface with incoming and outgoing electric field amplitudes. (b) Transmission spectrum of the metasurface with a square lattice of circular silicon nanodisks ($r = 150$ nm, $h = 220$ nm, $a = 1$ μm), and is assumed to be immersed in silica. In this figure the green solid line and yellow dotted line represent a 3D FDTD calculation and the theoretical fit (for the broader resonance), respectively. The inset shows similar theoretical fit for the sharper resonance. (c) Schematics of a meta-mirror Fabry-Perot cavity.

amplitudes evolve independently, as described earlier by the equations of a single metasurface. However, when the metasurfaces are brought together to form a FP cavity [as in Fig. 1(c)], the electric field amplitudes couple and interfere with each other. The temporal evolution of A_1 in the first metasurface can be written as $(dA_1/dt) = (j\omega_s - \Gamma)A_1 + c_s s_1 + c_s s_2'' + j\mu A_2$. Here, μ is the coupling coefficient that accounts for the mode coupling between the resonant modes of the two metasurfaces. The incoming electric field on the right side of the first metasurface, denoted as s_2'', can be expressed as $s_2'' = e^{-jkL} s_2'$. Here, kL, with $k = (n\omega/c)$ and n being the refractive index of the medium in which the system is inmersed, accounts for the phase accumulated by the transmitted wave from the second metasurface upon reaching the first metasurface, being s_2' the transmitted amplitude in the second metasurface [see Fig. 1(c) for details]. Based on the previous analysis of single metasurfaces, we deduce that $s_2' = e^{j\gamma} s_2 + c_a A_2$. Similarly, we can derive expressions for s_1' and s_1''. By eliminating all the internal amplitiudes (s_1', s_2', s_1'', and s_2''), we obtain the following equations describing the dynamics of the electric field amplitude in the bilayer metasurface system:

$$\frac{dA_1}{dt} = (j\omega_s - \Gamma)A_1 + c_s s_1 + c_s\left[e^{-jkL}(e^{j\gamma} s_2 + c_a A_2)\right] + j\mu A_2. \quad (1)$$

$$\frac{dA_2}{dt} = (j\omega_s - \Gamma)A_2 + c_s s_2 + c_s\left[e^{-jkL}(e^{j\gamma} s_1 + c_a A_1)\right] + j\mu A_1. \quad (2)$$

Equations (1) and (2) can be solved in the Fourier domain as

$$\begin{bmatrix} A_1 \\ A_2 \end{bmatrix} = c_s \begin{bmatrix} j\delta+\Gamma & e^{j(\gamma-kL)}\Gamma - j\mu \\ e^{j(\gamma-kL)}\Gamma - j\mu & j\delta+\Gamma \end{bmatrix}^{-1} \times \begin{bmatrix} 1 & e^{j(\gamma-kL)} \\ e^{j(\gamma-kL)} & 1 \end{bmatrix} \begin{bmatrix} s_1 \\ s_2 \end{bmatrix}. \quad (3)$$

The outgoing electric field from the left of the bilayer metasurface is $q_1 = e^{j\gamma}s_2'' + c_a A_1 = e^{j(2\gamma-kL)}s_2 + e^{j(\gamma-kL)}c_a A_2 + c_a A_1$. Similarly, the outgoing electric field from the right of the bilayer metasurface is given by $q_2 = e^{j\gamma}s_1'' + c_a A_2 = e^{j(2\gamma-kL)}s_1 + e^{j(\gamma-kL)}c_a A_1 + c_a A_2$. If we assume that the incident wave amplitude is s_1, then the power transmission coefficient, $T = T(\omega, L)$, can be derived using $T = |q_2/s_1|^2|_{s_2=0}$. The resulting expression can be evaluated by substituting the expressions of A_1 and A_2, and defining a normalized coupling coefficient $v \equiv [\mu(L)/\sqrt{\delta^2+\Gamma^2}]$. After some algebraic and trigonometric manipulations (see Supplemental Material [30]), it can be shown that

$$T(\omega, L) = \frac{\{|t_s|^2 - vG\}^2}{\{|t_s|^2 - vG\}^2 + 4|r_s|^2\{\sin(kL-\theta_s)-v\}^2}. \quad (4)$$

Here $G \equiv v - 2|r_s|\sin(\gamma - kL)$, $\theta_s(\omega) = \arg(t_s) - \arg(\delta) + \pi/2$, and the power reflection coefficient is given by $R = 1 - T$. Note that θ_s is a smooth and continuous function of ω and that, setting $v = 0$ in Eq. (4), this formula replicates results obtained by the scattering matrix method [32,33], which ignores evanescent interaction between the mirrors and assumes plane-wave-like propagation. Moreover, for $v = \theta_s = 0$, Eq. (4) recovers the transmission equation of a Fabry-Perot etalon with solid nonresonant mirrors.

In our study we consider FP cavities in which silicon metasurfaces [as described in Figs. 1(a) and 1(b)] act as mirrors. Figures 2(a) and 2(b) exhibit the transmission spectrum as a function of L of the metamirror FP cavities, near $\omega_s = 0.677(2\pi c/a)$ [i.e., the first transmission dip in Fig. 1(b)]. With $a = 1.0$ μm, this resonance frequency translates to a resonant wavelength of 1.477 μm. In Fig. 2(a) we render a 3D FDTD calculation, and in Fig. 2(b) we evaluate the transmission spectra by means of Eq. (4). The coupling coefficient μ [Fig. 2(c)] and the phase, $\gamma \cong 0.6\pi$, are both obtained by a numerical fitting method [34]. As seen in Fig. 2(c), the coefficient μ presents an exponential dependence with the cavity length, implying that the coupling between the two resonant modes is evanescent due to near-field coupling. On the other hand, both Figs. 2(a) and 2(b) present a very good agreement. Notice that the typical transmission spectra with dielectric thin film mirrors exhibit stripslike, periodic patterns of shallow ripples, and the depth

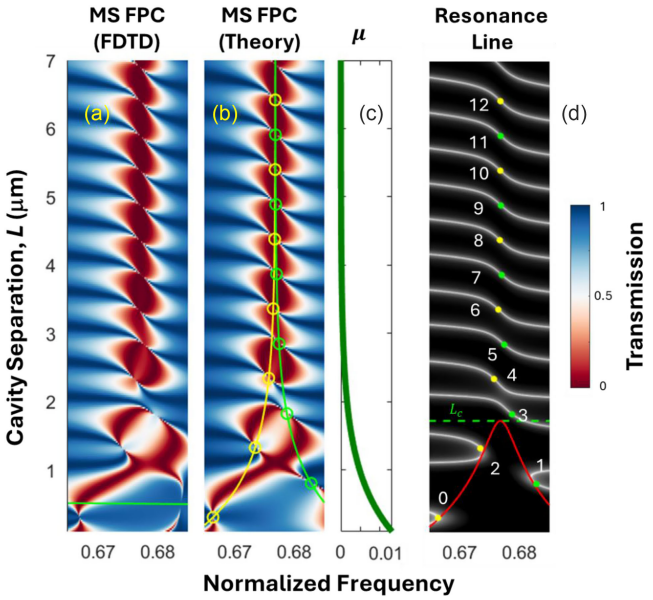

FIG. 2. Transmission spectra of Fabry-Perot cavities with dielectric resonant metasurface as mirrors. Spectra in (a) and (b) represent 3D FDTD and analytical [Eq. (4)] calculations, respectively. (c) Coupling coefficient $[\mu(L)]$ that accounts for the mode coupling. In (b), yellow and green lines represent $\omega_s \pm \mu(L)$, and the circles represent singular points. (d) White lines: Resonance lines obeying $\sin(kL - \theta_s) = v$. Dotted green line: $L = L_c$; Solid red line: locus of $\mu^2(L) = \delta^2 + \Gamma^2$. Dots with numbers: singular points and their order m [yellow: even m; green: odd m].

of the ripple increases with the dielectric constant of the mirror (see Fig. S3 of Supplemental Material [30] in which we have plotted the transmission spectra of FP cavities with silicon and dielectric film of averaged permittivity as mirrors). However, the transmission spectra of meta-mirror FP cavities significantly deviates from a striplike pattern. For very long L, where $v = 0$, there is a conservation of translational symmetry along the direction of L variation. In this scenario, a periodic pattern is observed in the transmission spectrum. However, Figs. 2(a) and 2(b) show that meta-mirror FP cavities exhibit periodic transmission lobes instead of strips. Moreover, the variation in transmission near the lobe region is very sharp, unlike the shallow ripplelike variations seen in the equivalent standard FP cavities. On the other hand, for shorter L in which $v > 0$, there is a clear disruption of translational symmetry. Consequently, in Figs. 2(a) and 2(b), we observe a nonperiodic transmission pattern for short meta-mirror FP cavities. In Fig. 2(b), we have also plotted the hypothetical lines (see Supplemental Material [30]) $\omega_s - \mu(L)$ and $\omega_s + \mu(L)$ [yellow and green lines in Fig. 2(b)], which clearly indicate the splitting of lobes for shorter cavities.

Physical insight on the numerical and semianalytical results rendered in Figs. 2(a) and 2(b) is gained by analyzing Eq. (4), looking for different mechanisms that

lead to transmission maxima. As in the case of standard FP cavities, the main resonant mechanism is associated with the constructive interference between reflected light at each mirror that leads to unity transmittance values, here with the additional ingredient of the coupling between the two metasurfaces, accounted for μ. In the case of meta-mirror FP cavities transmission resonances occurs when

$$\sin(kL - \theta_s) = v. \tag{5}$$

When there is no mode coupling between the two metasurfaces the above resonance condition simplifies to $2nL = (\lambda/\pi)\{m\pi + \theta_s(\omega)\}$, with m being an integer. In addition, if $\theta_s = 0$, we obtain the standard resonance condition of the usual Fabry-Perot cavity, $2nL = m\lambda$. Notice that in the case of meta-mirror FP cavities, the additional phase contribution $\theta_s(\omega)$ from the metasurface leads to a significant enhancement in the quality factor, despite having shorter cavity lengths, as we show below. Figure 2(d) renders the resonance lines [Eq. (5)] on the (ω, L) parameter space for the meta-mirror FP cavities analyzed in Figs. 2(a) and 2(b). In general, for a transmission resonance to occur we require $\sin(kL - \theta_s) = v < 1$. Hence, $\mu^2(L) < \delta^2 + \Gamma^2$. With $\delta = 0$, we can define a characteristic length, L_c such that $\mu(L_c) = \Gamma = (\omega_s/2Q_s)$. For the metasurface in Fig. 1(a), $L_c = 1.73\,\mu$m. In Fig. 2(d) we also show the boundary $\mu^2(L) = \delta^2 + \Gamma^2$ and the line $L = L_c$.

An interesting situation appears when $\sin(kL - \theta_s) = v$ and $|t_s|^2 = vG$, as both numerator and denominator in Eq. (4) vanish simultaneously. This situation corresponds to singular points in which transmission is also maximal, occurring within the resonance lines [white lines in Fig. 2(d)] at frequencies ω_m, and lengths L_m, such that $L_m = (c/n\omega_m)(\gamma + m\pi)$ (see Supplemental Material [30]). The corresponding singular frequencies $\omega_m = \omega_s - \mu(L_m)$ and $\omega_m = \omega_s + \mu(L_m)$ occur for even and odd integer values of m, respectively. In the neighborhood of these singular points, we expect ultrahigh quality factors as there is no decay mechanism apart from the intrinsic decay. In Figs. 2(b) and 2(d), we display the singular points of the meta-mirror FP cavities. As we can see from Fig. 2(b), transmission near the singular points changes rapidly. Note also that in standard FP cavities, the fundamental mode has $m = 1$ and the cavity length is $L = (\lambda/2n)$. In meta-mirror FP cavities, a singular point exists even for $m = 0$, with the corresponding cavity separation being $L_{m=0} = (\lambda/2n)(\gamma/\pi) < (\lambda/2n)$.

By looking at Fig. 2(d), distinct regimes as a function of L can be distinguished, depending on L being longer or shorter than L_c. For long cavities such that $L \gg L_c$ [i.e., $v = 0$], the equation of the resonance line is $L = (c/n\omega)[m\pi + \theta_s(\omega)]$. With ω being a slowly varying function compared to $\theta_s(\omega)$, the shape of L versus the ω curve follows very closely the shape of $\theta_s(\omega)$ [see resonance lines for $m > 5$ in Fig. 2(d)]. The resonance frequencies (ω_r) for any given L and order m can be calculated nonlinearly from the resonance line. In the vicinity of $\omega = \omega_s$, we can linearize $\theta_s(\omega)$ as $\theta_s(\omega) = \theta_s(\omega_s) + (\omega - \omega_s)\tau_g(\omega_s)$, where $\tau_g(\omega_s) = [d\theta_s(\omega)/d\omega]|_{\omega=\omega_s} = -(2Q_s/\omega_s)$ is the group delay. Hence, near the mth singular point, we can use the following linear relationship,

$$2nL = \left(m + \frac{\gamma}{\pi}\right)\lambda + \frac{2Q_s}{\pi}(\lambda - \lambda_s). \tag{6}$$

Right at $\lambda = \lambda_s$, we have the singular point. For the transmission characteristics near resonance in the case $v = 0$, we can apply a small angle approximation (see Supplemental Material [30]) to show

$$T(\omega, L) = \frac{|t_s(\omega_r)|^4}{|t_s(\omega_r)|^4 + 4|r_s(\omega_r)|^2\left[\frac{nL}{c} - \tau_g(\omega_r)\right]^2[\omega - \omega_r]^2}. \tag{7}$$

Equation (7) has a Lorentzian line shape, with the quality factor for resonant peaks given by

$$Q = \sqrt{F}\left[\frac{\pi nL}{\lambda_r} + Q_s\right] = Q_L + Q_M. \tag{8}$$

Here, $F = 4|r_s(\omega_r)|^2/|t_s(\omega_r)|^4$ is the coefficient of finesse. F, being a huge number that traditionally measures the sharpness of the interference fringes. In Eq. (8), the first term $Q_L = (\pi nL/\lambda_r)\sqrt{F}$ represents the length-dependent quality factor of the meta-mirror FP cavity, which is also the total quality factor in standard FP cavities. However, the second term, $Q_M = Q_s\sqrt{F}$, is unique for meta mirrors and it is length independent. This is an important result as it shows that in meta-mirror FP cavities, there are two mechanisms, Q_L and Q_M, that feed the quality factor. From the derivations, we can see that Q_L results from the length-dependent phase term, and Q_M originates from the phase contribution of the metasurface. Thanks to this additional term Q_M, cavity lengths to achieve the same Q can be much shorter in metal-mirror FP cavities than in traditional ones. In Sec. II and Fig, S1 of the Supplemental Material [30], we provide a detailed discussion of the quality factors for meta-mirror FP cavities and compare them with those of traditional cavities. From Eq. (8), we can also define a second characteristic length, $L_Q \equiv \lambda_s(Q_s/\pi n) > L_c$, which marks the shift in quality factor domination from Q_M to Q_L. For the particular metasurface utilized in our study, $L_Q \cong 51\,\mu$m. For very long cavities such that $L \gg L_Q, Q_L$ dominates with $Q \approx Q_L$. Conversely, for shorter cavities, such that $L_c < L < L_Q$, we have $Q_M \gg Q_L$, and hence Q_M

dominates with $Q \approx Q_M$. Therefore, even in the limit $v = 0$ in which the coupling between the metasurfaces is negligible, a bilayer system creates an induced transparency configuration [35,36], different to that observed in traditional FP cavities. Significantly, when $L_c < L < L_Q$, the quality factor of the transmission peak is proportional to $Q_s\sqrt{F}$. Note also that, as $\omega_r \to \omega_s$, $t_s \to 0$, and hence the coefficient of finesse F increases sharply. Quality factor of single metasurface Q_s can be engineered to achieve very high values. In the literature, there are many reports with single metasurface of quality factors ranging between 10^2–10^5. Thus, with an additional multiplication factor $\sqrt{F}$, meta-mirror FP cavities can support resonant transmission peaks presenting ultrahigh quality factors. In Fig. S2 of the Supplemental Material [30], we further illustrate how these quality factors can be tuned by altering the geometrical parameters of the metasurface.

In the other regime of short cavities ($L < L_c$), the earlier-described resonance [associated with θ_s in Eq. (5)] for longer cavities is intertwined by the effect of the mode coupling between the metasurfaces. Thus, meta-mirror FP cavities in this regime exhibit different resonance and transmission characteristics. First, the singularity points deviate from $\omega_m = \omega_s$ to $\omega_m = \omega_s \pm \mu(L_m)$. Thus, the resonance line breaks and become discontinuous at $\omega = \omega_s$, giving rise to a significantly different shape when compared to that for $L > L_c$ [see Fig. 2(d)]. A resonance-free region in the (ω, L) parameter space is created in the neighborhood of $\omega = \omega_s$ when $\mu^2 > \delta^2 + \Gamma^2$, as Eq. (5) cannot be fulfilled. Let $\omega = \omega_r$ to be the solution $\sin(kL - \theta_s) = v$ [Eq. (5)] so we have $T(\omega_r) = 1$. If $\omega = \omega_{r'} \neq \omega_r$ is the solution $|t_s|^2 = vG(v, L)$ [i.e., vanishing numerator of Eq. (4)], then we have $T(\omega_{r'}) = 0$ (i.e., a dip). If $\omega_r - \omega_{r'} > 0$, then in the transmission spectrum a transmission peak will be followed by a transmission dip. Transmission toggles the other way around if $\omega_r - \omega_{r'} < 0$. When, ω_r and $\omega_{r'}$ come close to each other, this directional transmission switching occurs in a narrow frequency region, resulting in a Fano resonance. As the discrepancy between two frequencies shrinks, the sharpness of the Fano resonance increases, and finally when $\omega_r = \omega_{r'} = \omega_m$, we have a singularity.

Figure 3 renders the electric and magnetic field densities in both short ($L = 1.2\ \mu\text{m} < L_c$) and long ($L = 4.3\ \mu\text{m} > L_c$) cavities. For the shorter cavity case [$L = 1.2\ \mu\text{m}$], the field pattern clearly shows a stronger interaction. Nevertheless, in both cases, the electromagnetic fields concentrate primarily on the metasurfaces region rather than at the middle of the cavity. The significant group delay exhibited by the metasurface leads to a notable shift in the concentration of the electromagnetic field from the centre of the FP cavity towards the metasurface region. As shown earlier, this shift contributes to a remarkable enhancement in the quality factor of the FP resonances.

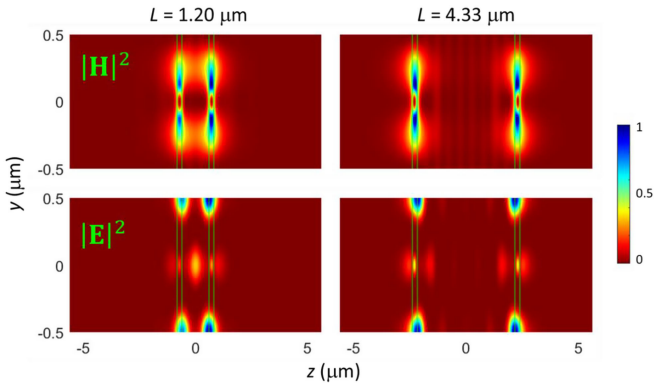

FIG. 3. Electric and magnetic field densities of FP meta-mirror cavities for two representative cases.

In summary, we have presented the optical properties of FP cavities with dielectric resonant metasurfaces as mirrors. By using a temporal couple mode formalism, we derive the transmission characteristics supported by these systems. There are three cavity length regimes based on the nature and quality of the resonance. These regions are marked by two characteristic cavity lengths (L_c and L_Q). The first regime ($L_c > L$) exhibits Fano resonances. The second and third regimes display induced transparencies with Lorentzian line shapes. The second regime's ($L_c < L < L_Q$) resonance sharpness is primarily governed by the quality factor of the single metasurface, allowing for sharp resonances even with shorter cavities. In contrast, the third regime ($L > L_Q$) is predominantly controlled by the cavity length itself. Furthermore, in FP meta-mirror cavities, resonances happen even for cavity separations that are smaller than the cavity length of the fundamental mode in traditional FP cavities.

[1] C. Zhao Saavedra, D. Pandey, W. Alt, D. Meschede, and H. Pfeifer, Spectroscopic gas sensor based on a fiber Fabry-Perot cavity, Phys. Rev. Appl. **18**, 044039 (2022).
[2] V. Z. Tronciu, H. J. Wünsche, M. Wolfrum, and M. Radziunas, Semiconductor laser under resonant feedback from a Fabry-Perot resonator: Stability of continuous-wave operation, Phys. Rev. E **73**, 046205 (2006).
[3] B. Zhou, H. Jiang, R. Wang, and C. Lu, Optical fiber fiber Fabry-Perot filter with tunable cavity for high-precision resonance wavelength adjustment, J. Lightwave Technol. **33**, 2950 (2015).
[4] M. Celik, E. Şahin, T. Yandayan, R. Hamid, A. Akgöz, B. Özgür, M. Çetintaş, and A. Demir, Application of the differential Fabry-Perot interferometer in angle metrology, Meas. Sci. Technol. **27**, 035201 (2016).
[5] H. T. Kim, W. Hwang, Y. Liu, and M. Yu, Ultracompact gas sensor with metal-organic-framework-based differential fiber-optic Fabry-Perot nanocavities, Opt. Express **28**, 29937 (2020).

[6] M. Wilkens, E. Goldstein, B. Taylor, and P. Meystre, Fabry-Pérot interferometer for atoms, Phys. Rev. A **47**, 2366 (1993).
[7] F. J. Bailén, D. Orozco Suárez, and J. C. del Toro Iniesta, Fabry-Pérot etalons in solar astronomy. A review, Astrophys. Space Sci. **368**, 55 (2023).
[8] Jie Hu, Bandyopadhyay Sankhyabrata, Liu Yu-hui, and Shao Li-yang, A review on metasurface: From principle to smart metadevices, Front. Phys. **8**, 586087 (2021).
[9] Hou-Tong Chen, Antoinette J. Taylor, and Nanfang Yu, A review of metasurfaces: Physics, and applications, Rep. Prog. Phys. **79**, 076401 (2016).
[10] Shuming Wang, Pin Chieh Wu, Vin-Cent Su, Yi-Chieh Lai, Mu-Ku Chen, Hsin Yu Kuo, Bo Han Chen *et al.*, A broadband achromatic metalens in the visible, Nat. Nanotechnol. **13**, 227 (2018).
[11] Mohammadreza Khorasaninejad and Federico Capasso, Broadband multifunctional efficient meta-gratings based on dielectric waveguide phase shifters, Nano Lett. **15**, 6709 (2015).
[12] Guoxing Zheng, Holger Mühlenbernd, Mitchell Kenney, Guixin Li, Thomas Zentgraf, and Shuang Zhang, Metasurface holograms reaching 80% efficiency, Nat. Nanotechnol. **10**, 308 (2015).
[13] Zi Wang, Yahui Xiao, Kun Liao, Tiantian Li, Hao Song, Haoshuo Chen, S. M. Zia Uddin *et al.*, Metasurface on integrated photonic platform: From mode converters to machine learning, Nanophotonics **11**, 3531 (2022).
[14] Rao Fu, Kuixian Chen, Zile Li, Shaohua Yu, and Guoxing Zheng, Metasurface-based nanoprinting: Principle, design, and advances, Opto-Electron. Sci. **1**, 220011 (2022).
[15] Patrice Genevet, Federico Capasso, Francesco Aieta, Mohammadreza Khorasaninejad, and Robert Devlin, Recent advances in planar optics: From plasmonic to dielectric metasurfaces, Optica **4**, 139 (2017).
[16] Seyedeh Mahsa Kamali, Ehsan Arbabi, Amir Arbabi, and Andrei Faraon, A review of dielectric optical metasurfaces for wavefront control, Nanophotonics **7**, 1041 (2018).
[17] Wenhong Yang, Shumin Xiao, Qinghai Song, Yilin Liu, Yunkai Wu, Shuai Wang, Jie Yu, Jiecai Han, and Din-Ping Tsai, All-dielectric metasurface for high-performance structural color, Nat. Commun. **11**, 1864 (2020).
[18] Z. Wang *et al.*, Metasurface on integrated photonic platform: From mode converters to machine learning, Nanophotonics **11**, 3531 (2022).
[19] H. Huang, A. C. Overvig, Y. Xu, S. C. Malek, C.-C. Tsai, A. Alù, and N. Yu, Leaky-wave metasurfaces for integrated photonics, Nat. Nanotechnol. **18**, 580 (2023).
[20] A. M. Shaltout, J. Kim, A. Boltasseva, V. M. Shalaev, and A. V. Kildishev, Ultrathin and multicolour optical cavities with embedded metasurfaces, Nat. Commun. **9**, 2673 (2018).
[21] J. Flannery, R. A. Maruf, T. Yoon, and M. Bajcsy, Fabry-Pérot cavity formed with dielectric metasurfaces in a hollow-core fiber, ACS Photonics **5**, 337 (2018).
[22] Wenwei Liu, Zhancheng Li, Hua Cheng, and Shuqi Chen, Dielectric resonance-based optical metasurfaces: From fundamentals to applications, Iscience **23**, 101868 (2020).
[23] Kirill Koshelev and Yuri Kivshar, Dielectric resonant metaphotonics, ACS Photonics **8**, 102 (2020).
[24] Isabelle Staude, Andrey E. Miroshnichenko, Manuel Decker, Nche T. Fofang, Sheng Liu, Edward Gonzales, Jason Dominguez *et al.*, Tailoring directional scattering through magnetic and electric resonances in subwavelength silicon nanodisks, ACS Nano **7**, 7824 (2013).
[25] John D. Joannopoulos, Steven G. Johnson, Joshua N. Winn, and Robert D. Meade, *Photonic Crystals: Molding the Flow of Light*, 2nd Ed. (Princeton University Press, Princeton, NJ, 2008), REV-Revised, 2, Chap. 10.
[26] W. Suh, Z. Wang, and S. Fan, Temporal coupled-mode theory and the presence of non-orthogonal modes in lossless multimode cavities, IEEE J. Quantum Electron. **40**, 1511 (2004).
[27] S. Fan, W. Suh, and J. D. Joannopoulos, Temporal coupled-mode theory for the Fano resonance in optical resonators, J. Opt. Soc. Am. A **20**, 569 (2003).
[28] Q. Li, T. Wang, Y. Su, M. Yan, and M. Qiu, Coupled mode theory analysis of mode-splitting in coupled cavity system, Opt. Express **18**, 8367 (2010).
[29] C. Manolatou, M. J. Khan, S. Fan, P. R. Villeneuve, H. A. Haus, and J. D. Joannopoulos, Coupling of modes analysis of resonant channel add-drop filters, IEEE J. Quantum Electron. **35**, 1322 (1999).
[30] See Supplemental Material at http://link.aps.org/supplemental/10.1103/PhysRevLett.133.226901 for details of derivations, and numerical examples.
[31] Allen Taflove, *Computational Electromagnetics: The Finite-Difference Time-Domain Method* (Artech House, Boston, 2005), FDTD: 3D Electromagnetic Simulator, Lumerical Inc.
[32] L. A. Coldren, S. W. Corzine, and M. L. Mashanovitch, *Diode Lasers and Photonic Integrated Circuits* (John Wiley & Sons, New York, 2012), Chap. 3.
[33] D. R. Smith, D. C. Vier, T. Koschny, and C. M. Soukoulis, Electromagnetic parameter retrieval from inhomogeneous metamaterials, Phys. Rev. E **71**, 036617 (2005).
[34] https://www.mathworks.com/help/matlab/ref/fminbnd.html; https://www.mathworks.com/help/matlab/ref/min.html.
[35] S. E. Harris, Electromagnetically induced transparency in an ideal plasma, Phys. Rev. Lett. **77**, 5357 (1996).
[36] David D. Smith, Hongrok Chang, Kirk A. Fuller, A. T. Rosenberger, and Robert W. Boyd, Coupled-resonator-induced transparency, Phys. Rev. A **69**, 063804 (2004).